

Dinuclear Quinonoid-Bridged d⁸ Metal Complexes with Redox-Active Azobenzene Stoppers: Electrochemical Properties and Electrochromic Behavior

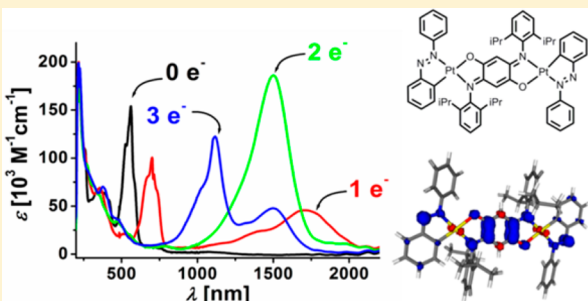
Naina Deibel,^{†,‡} Michael G. Sommer,[‡] Stephan Hohloch,[‡] Johannes Schwann,[‡] David Schweinfurth,[‡] Fabian Ehret,[†] and Biprajit Sarkar^{*,‡}

[†]Institut für Anorganische Chemie, Universität Stuttgart, Pfaffenwaldring 55, D-70569 Stuttgart, Germany

[‡]Institut für Chemie und Biochemie, Freie Universität Berlin, Fabeckstraße 34-36, D-14195 Berlin, Germany

Supporting Information

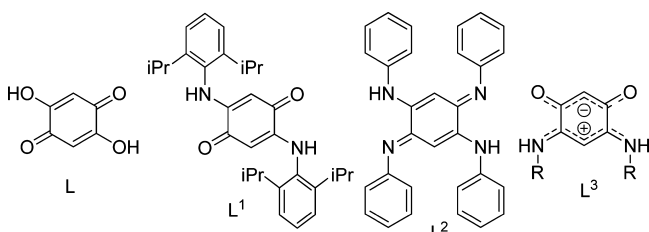
ABSTRACT: The ligands 2,5-bis[2,6-(diisopropyl)anilino]-1,4-benzoquinone (L^1) and azophenine (L^2) were reacted with $[(az_H)M(\mu-Cl)_2M(az_H)]$ ($M = Pd, Pt$, $az = azobenzene$) to generate the complexes $[(az_H)Pd(\mu-L_{2H}^1)Pd(az_H)]$ (**1**), $[(az_H)Pt(\mu-L_{2H}^1)Pt(az_H)]$ (**2**), and $[(az_H)Pt(\mu-L_{2H}^2)Pt(az_H)]$ (**3**). Structural characterization of **1** and **2** revealed a distorted-square-planar environment around the metal centers, localization of double bonds within the L_{2H}^1 ligand, and binding of L_{2H}^1 to the metal centers through anionic O⁻ and neutral imine type donors. Furthermore, the N=N double bond within az_H displayed a slight elongation in comparison to that in free az owing to back-bonding from the d π metal orbitals to the π^* orbitals of az_H . All complexes show an irreversible oxidation step and three stepwise, reversible one-electron-reduction steps in their cyclic voltammograms. The redox potentials of the complexes are seen to be strongly dependent on the nature of the bridging ligand. UV-vis-near-IR spectroelectrochemical measurements show that these complexes are strongly absorbing in the visible or the near-IR region, depending on the charged state of the metal complexes. The position and intensity of the absorption bands can be tuned by varying the bridging ligand and the metal center. Additionally, the absorption bands can be tuned by simple one-electron-transfer steps. EPR spectroelectrochemistry and DFT calculations have been used to shed light on the electronic structures of these metal complexes in their various redox states and to interpret the results obtained from the UV-vis-near-IR spectroelectrochemistry measurements. In this work, a comparison is being made among d⁸ metal complexes containing bridging quinones with a [O,O,O,O], [O,N,O,N], or [N,N,N,N] donor set, and the advantages of using the isoelectronic [NR] for [O] substitution on the quinonoid ligands for generating electrochromic metal complexes are discussed. In doing so, we also present complex **3**, which is a rare example of a dinuclear metal complex containing the azophenine bridge.



INTRODUCTION

Quinones are examples of typical noninnocent ligands.¹ Metal complexes of quinones have been historically investigated because of their fascinating electronic structures.² More recently metal complexes of quinone ligands have been used for bond activation reactions and catalysis.³ The most widely used quinonoid ligand that is capable of bridging two metal centers is 2,5-dihydroxy-1,4-benzoquinone (L ; Chart 1). Metal complexes with L or its various deprotonated forms have been investigated with respect to their chemical and physical properties.⁴ Despite the widespread use of L in coordination and organometallic chemistry, tuning of steric and electronic properties in L is rather limited. Thus, in recent years, we⁵ and others⁶ have developed several new synthetic routes for generating potentially bridging quinone ligands where one or more of the [O] donors in L have been substituted by the isoelectronic [NR] group. The advantages of this approach for tuning the electronic and electrochemical properties of the corresponding metal complexes, and for inducing chemical

Chart 1. Ligand L and Related Ligands Containing [NR] Groups



reactivity in and with them, have been documented.⁶ Such efforts have led to the development of ligands such as 2,5-bis[2,6-(diisopropyl)anilino]-1,4-benzoquinone) (L^1 ; Chart 1).⁶ⁱ

Special Issue: Organometallic Electrochemistry

Received: January 14, 2014

Published: April 24, 2014



Additionally, azophenine (L^2 ; Chart 1) is an all-nitrogen-donating ligand that has been known for decades.⁷ Despite this fact, metal complexes of L^2 have only been sporadically reported.^{6d,m,8} Recently, we have shown the advantages of using L^2 as a bridge for inducing spin–spin coupling in dicopper(II) complexes in comparison to its [O]-containing counterparts.^{5e} Others have used a diiron complex of L^2 for investigating radical-bridged spin–spin coupling.^{8e}

During the course of our investigations of metal complexes of such potentially bridging quinonoid ligands, we discovered that these metal complexes display highly electrochromic behavior in the visible as well as the near-IR region.⁹ Following up on a recent work of ours on Pt(II) complexes with the ligands of type L^3 (Chart 1),^{5k} we present here the complexes $[(az_{-H})Pd(\mu-L^1_{-2H})Pd(az_{-H})]$ (**1**), $[(az_{-H})Pt(\mu-L^1_{-2H})Pt(az_{-H})]$ (**2**), and $[(az_{-H})Pt(\mu-L^2_{-2H})Pt(az_{-H})]$ (**3**), where az is azobenzene. Pd(II) and Pt(II) complexes of az_{-H} have been investigated for electrochemical properties, for switchable functions, and for elucidating the protonation/deprotonation process at az/az_{-H} .¹⁰ The advantages of using the [NR] for [O] isoelectronic substitution in quinonoid ligands for generating electrochromic metal complexes are discussed. A combination of electrochemistry, spectroelectrochemistry, and DFT calculations are used to elucidate the electronic structures of the metal complexes in their various redox states and to understand their electrochromic behavior.

■ RESULTS AND DISCUSSION

Synthesis and Crystal Structures. The precursor $[(az_{-H})M(\mu-Cl)_2M(az_{-H})]$ ($M = Pd, Pt$),¹¹ which was one of the first examples of ortho metalation in Pd(II) and Pt(II) complexes, was used in this work for synthesizing the metal complexes. Reactions of $[(az_{-H})Pd(\mu-Cl)_2Pd(az_{-H})]$ or $[(az_{-H})Pt(\mu-Cl)_2Pt(az_{-H})]$ with L^1 in the presence of NEt_3 led to the formation of **1** and **2**, respectively (see the Experimental Section). The reaction of $[(az_{-H})Pt(\mu-Cl)_2Pt(az_{-H})]$ with L^2 in the presence of NEt_3 led to the formation of **3** (Chart 2). Even though the formation of various

reactions delivered solids that were insoluble in all tested organic solvents. Hence, those substances could not be characterized further. It is thus seen that the success of isolating pure compounds which can be well characterized in solution is strongly dependent on the [NR] groups present at the quinonoid ligand, with the best results being obtained for the ligand L^1 .

While using the ligand L^3 , we were able to isolate Pt(II) complexes where az in its mono- and dideprotonated forms either binds to one metal center or acts as a bridging ligand in a dinuclear complex.^{5k} In those cases, L^3 could be deprotonated only once, and hence it was bound to only one metal center. In the present case, the ligands L^1 and L^2 readily act as bridging ligands. Ligands such as L^1 readily form bridges, as it is easy to doubly deprotonate them.^{5a–e} For L^3 , the monodeprotonated form is easily generated, and it tends to resist the removal of a further proton.^{5f–k} These are established differences between the “para” (L^1) and the “meta” (L^3) forms of such ligands. For L^2 , the presence of a base is usually seen to remove two protons as well as lead to the formation of an L^2_{-2H} -bridged dinuclear complex.^{5e}

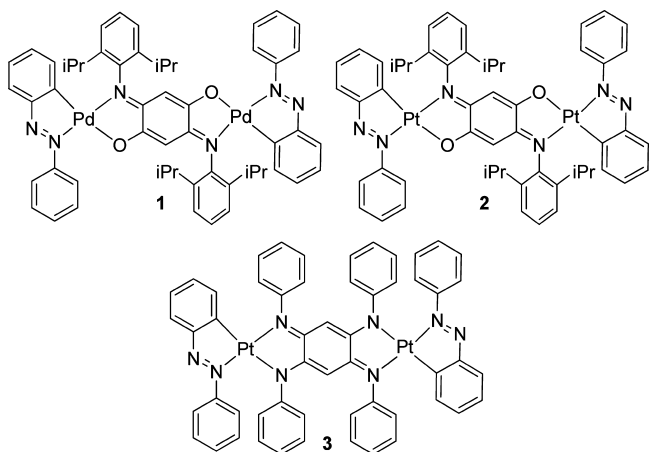
All of the complexes were characterized by 1H and ^{13}C NMR spectroscopy, mass spectrometry, and elemental analysis, and these measurements established the formation and purity of the complexes (see the Experimental Section).

Single crystals of both **1** and **2** were obtained that were suitable for X-ray diffraction studies. **1** crystallizes as $1\text{-}2Et_2O$ in the monoclinic $P2_1/n$ space group and **2** in the triclinic $P\bar{1}$ space group (Table S1 (Supporting Information)). Despite several attempts, we were not able to obtain suitable single crystals of **3** for X-ray diffraction studies. However, NMR and mass spectrometry studies clearly establish the composition and structure of that complex.

The metal centers in both **1** and **2** are in a distorted-square-planar environment (Figure 1), the distortion being caused by the chelating nature of the ligands L^1_{-2H} and az_{-H} . The distortion can be readily seen, for instance, from the O1–Pd–N1 angle of $78.8(1)^\circ$ in **1** (Table 1). The Pd–C20 and Pt–C20 distances to the C[–] donor of az_{-H} are the shortest metal–ligand bond lengths in both complexes (Table 1). Accordingly, the Pd–O1 and Pt–O1 bond lengths to the O donor that is trans to the carbanionic donor are relatively long possibly because of trans influence.

A look at the bond lengths within L^1_{-2H} in both **1** and **2** delivers some interesting trends. The C1–O1 bond at about 1.28 Å is closer to a C–O single-bond length, and the C2–N1 bond length at 1.32 Å is closer to a C=N double-bond length. Accordingly, C1–C3 at 1.37 Å is shorter than C2–C3 at 1.41 Å. Thus, the best localized description of the bridge L^1_{-2H} is of a “dimino-dialkoxy” donor type, with the negative charge possibly being better stabilized at the more electronegative O atom. Similar observations have been made in dinuclear complexes of ligands such as L^1_{-2H} with other metal centers.^{5a–e} The C1–C2 bond length of 1.5 Å fits with a single bond. Hence, these bridging ligands have localized double bonds in the “upper” and “lower” parts of the molecule that are connected by C–C single bonds. The azo N2–N3 bond length is about 1.27 Å in both complexes and is slightly longer than what is expected for a normal N=N azo double bond. This elongation is likely related to π back-bonding from filled $d\pi$ orbitals of Pd(II) or Pt(II) to the empty π^* orbital of az_{-H} .^{5k,10e} The metal centers and the ligand donor atoms are almost coplanar in both complexes, with the dihedral angle between the planes formed by C20–C19–N3–N2–M and M–O1–C1–C2–N1 being 6.9° . The uncoordinated phenyl rings of the az_{-H} ligand are twisted with respect to this plane with dihedral angles of 35.3 and 47.1° for **1** and **2**, respectively. Similarly, the diisopropylphenyl rings at the L^1_{-2H} ligand are

Chart 2. Complexes Synthesized in This Work



geometrical isomers is possible for such complexes, we were able to detect only one isomer with our synthetic methods. Unfortunately, attempts to synthesize a Pd(II) complex with the deprotonated form of L^2 only led to poorly defined mixtures from which no pure complex could be isolated.

Attempts were made to react the precursors $[(az_{-H})M(\mu-Cl)_2M(az_{-H})]$ ($M = Pd, Pt$) with the all-oxygen-donating ligand L . Those

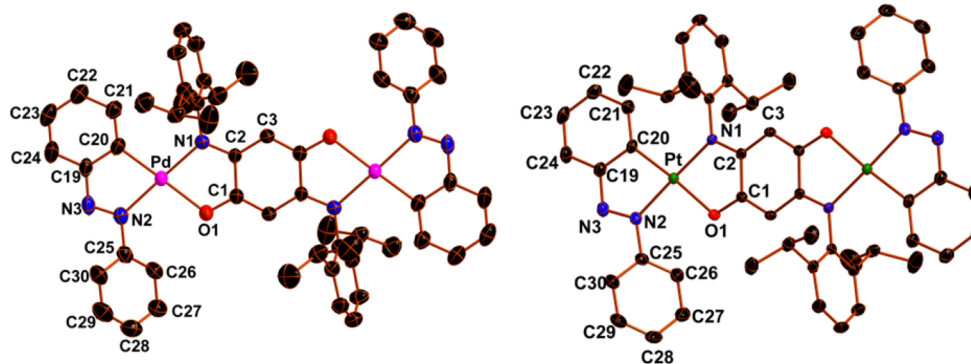


Figure 1. ORTEP plots of **1**·2Et₂O (left) and **2** (right). Ellipsoids are drawn at the 50% probability level. Hydrogen atoms and solvent molecules have been omitted for clarity.

Table 1. Selected Bond Lengths (Å) and Bond Angles (deg) of 1·2Et₂O and 2

	1·2Et ₂ O	2
M—O1	2.100(3)	2.095(2)
M—N1	2.046(3)	2.024(2)
M—C20	1.994(4)	1.989(2)
M—N2	2.036(4)	1.989(2)
C1—O1	1.286(4)	1.287(3)
C1—C2	1.504(5)	1.498(3)
C2—C3	1.411(5)	1.405(3)
C1—C3	1.368(5)	1.376(3)
C2—N1	1.324(4)	1.322(3)
N2—N3	1.267(5)	1.274(3)
N3—C19	1.396(6)	1.392(3)
C19—C20	1.415(6)	1.415(4)
C20—C21	1.380(6)	1.394(4)
C21—C22	1.398(6)	1.393(4)
C22—C23	1.383(8)	1.386(4)
C23—C24	1.378(8)	1.379(4)
C24—C19	1.394(6)	1.398(4)
M—M	7.975(2)	7.95(3)
O1—M—N1	78.8(1)	78.71(7)
N1—M—C20	102.5(2)	104.72(9)
C20—M—N2	78.9 (2)	78.33(9)
N2—M—O1	100.0(1)	98.09(8)
N1—M—N2	174.6(1)	175.23(8)
C20—M—O1	178.4(1)	175.75(8)

twisted with respect to the central quinone ring with dihedral angles of 75.5 and 81.4° for **1** and **2**, respectively. The intramolecular metal–metal distance in both complexes is about 8 Å.

Cyclic Voltammetry. The presence of redox-active azo stoppers and redox-active bridging quinonoid ligands in these complexes is likely to make such compounds redox-rich. To probe this fact, the cyclic voltammetry of all three complexes was investigated in THF/0.1 M Bu₄NPF₆ as well as in CH₂Cl₂/0.1 M Bu₄NPF₆. THF was used as a solvent to provide for a larger potential window on the reductive side, and CH₂Cl₂ was used to get a larger window on the oxidative side. The complexes **1** and **2** each display a quasi-reversible oxidation step at around 0.8 V vs the Fc/Fc⁺ couple (Figure S1 (Supporting Information)). The quasi-reversible behavior is seen from the different current heights for the anodic and cathodic peaks. The reversibility did not improve on going to higher scan rates. Changing the metal

center does not seem to have much influence on the oxidation potentials of **1** and **2**. The diplatinum complex **3**, which contains the deprotonated form of azophenine as a bridge, displays two oxidation steps, both of which are electrochemically irreversible. The oxidation potentials in **3** are strongly cathodically shifted in comparison to those of its diplatinum analogue **2**, which contains a different quinonoid bridge (Table 2).

Table 2. Electrochemical Data of the Complexes from Cyclic Voltammetry

compd	<i>E</i> ^{ox2} (V)	<i>E</i> ^{ox1} (V)	<i>E</i> ^{red1} (V)	<i>E</i> ^{red2} (V)	<i>E</i> ^{red3} (V)
1			-1.50 ^a	-1.64 ^a	-2.09 ^a
	0.75 ^{b,c}	-1.59 ^b	-1.72 ^b		
2			-1.16 ^a	-1.57 ^a	-2.03 ^a
	0.81 ^{b,c}	-1.27 ^b	-1.64 ^b		
3			-1.70 ^a	-2.00 ^a	-2.54 ^a
	0.72 ^{b,c}	0.19 ^{b,c}	-1.42 ^b	-1.69 ^b	

^aHalf-wave potentials from cyclic voltammetric measurements in THF/0.1 M Bu₄NPF₆ for reversible processes at 298 K and a scan rate of 100 mV s⁻¹. Ferrocene/ferrocenium was used as an internal standard. ^bHalf-wave potentials from cyclic voltammetric measurements in CH₂Cl₂/0.1 M Bu₄NPF₆ for reversible processes at 298 K and a scan rate of 100 mV s⁻¹. Ferrocene/ferrocenium was used as an internal standard. ^c*E*_{pa} for the irreversible process.

Complexes **1**–**3** display three reduction steps in THF/0.1 M Bu₄NPF₆, all of which are reversible (Figure 2). In CH₂Cl₂/0.1 M

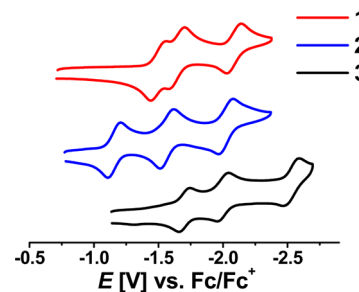


Figure 2. Cyclic voltammograms of the complexes in THF/0.1 M Bu₄NPF₆ at 298 K. Scan rate: 100 mV/s.

Bu₄NPF₆ only two reduction steps are observed (Figure S1 (Supporting Information)). The position of the individual redox steps and the potential difference between the various redox steps within a complex depend on the metal center as well as the bridging ligand used (Figure 2 and Table 2). On comparison of **1**

and **2**, which have the same bridging ligand but different metal centers, it is seen that the potential for the first reduction step for the dipalladium complex **1** is strongly cathodically shifted in comparison to its diplatinum analogue **2**. The second and third reduction steps for both these complexes occur almost at the same potentials (Figure 2). As a result, the comproportionation constant K_c ($K_c = 10^{\Delta E/59}$, ΔE in mV), which determines the thermodynamic stability of a particular redox state, is on the order of only 10^2 for $\mathbf{1}^{\bullet-}$ but 10^6 for $\mathbf{2}^{\bullet-}$. The thermodynamic stability of the one-electron-reduced form is thus seen to be higher for the diplatinum complex in comparison to the dipalladium complex when the same bridging ligand is used. On comparison of complexes **2** and **3**, which have the same metal centers but bridges with $[\text{O},\text{N},\text{O},\text{N}]$ and $[\text{N},\text{N},\text{N},\text{N}]$ donor atoms, respectively, it is seen that all reduction potentials are cathodically shifted for **3** in comparison to **2**. This is likely an effect of the electronegativity difference of the donor atoms. The K_c value for $\mathbf{3}^{\bullet-}$ is on the order of 10^5 and is thus slightly smaller than the value for $\mathbf{2}^{\bullet-}$. The potential differences between the second and third reduction steps are in similar ranges for all three complexes (Table 2). It can also be seen from Table 2 that the solvent (CH_2Cl_2 vs THF) has some influence on the redox potentials of these complexes, a fact that is well established in molecular electrochemistry.¹²

For comparison, the complex $[(\text{L}^{\text{3}-\text{H}})\text{Pt}(\mu\text{-az}_{\text{2H}})\text{Pt}(\text{L}^{\text{3}-\text{H}})]$, which has a doubly deprotonated azobenzene bridge and a monodeprotonated L^{3} (Chart 1) ligand as a stopper, displays three reversible reduction steps at -1.08 , -1.62 , and -1.94 V in $\text{CH}_2\text{Cl}_2/0.1$ M Bu_4NPF_6 .^{5k} From the above discussion, it can thus be seen that the metal center does not seem to have much of an influence on the oxidation potentials of these complexes. However, the oxidation potentials are strongly dependent on the nature of the bridging ligand. The reduction potentials seem to be dependent on the metal centers as well as on the bridging ligand. In order to shed light on the individual redox states that can be generated by stepwise reduction of these complexes and to elucidate their electronic structure, a combination of UV-vis-near-IR and EPR spectroelectrochemistry and DFT calculations were used.

EPR Spectroscopy and Spin-Density Calculations. The oxidation steps for all of the complexes presented here are either chemically and electrochemically irreversible or quasi-reversible, and hence the oxidation step for the complexes will not be discussed further. The in situ generated one-electron-reduced forms $\mathbf{1}^{\bullet-}$, $\mathbf{2}^{\bullet-}$, and $\mathbf{3}^{\bullet-}$ display EPR signals in THF/0.1 M Bu_4NPF_6 at 298 K with g values of 1.998, 1.982, and 1.984, respectively (Figure 3 and Figure S2 (Supporting Information)). The peak-to-peak separations of the signals are 12, 10, and 12 G for $\mathbf{1}^{\bullet-}$, $\mathbf{2}^{\bullet-}$, and $\mathbf{3}^{\bullet-}$, respectively. Except for $\mathbf{1}^{\bullet-}$, where poorly resolved hyperfine coupling to certain nuclei starts to show up, no hyperfine splitting was observed for the other two complexes. This is possibly due to unfavorable hyperfine coupling constant to line width ratios. The observance of the signals in fluid solutions at 298 K, the g values which are close to the g value of the free electron, and the narrow width of the signals all point to a predominantly ligand-centered spin.¹³ However, in the absence of information from hyperfine coupling, no prediction about specific spin density distribution can be directly made from the EPR results.

In the absence of hyperfine coupling data from EPR spectroscopy, we turned to spin density calculations at the DFT level to decipher the spin situation within the one-electron-reduced species. Calculations were carried out on **1** and **2**, and

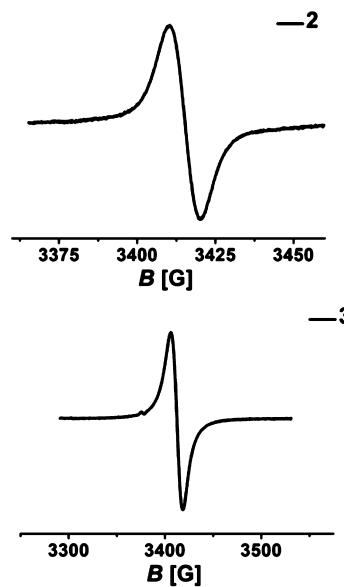


Figure 3. EPR spectra of in situ generated $\mathbf{2}^{\bullet-}$ and $\mathbf{3}^{\bullet-}$ in THF/0.1 M Bu_4NPF_6 at 298 K.

their one-electron-reduced forms as experimental crystal structures are available only for **1** and **2**. Structure optimization was carried out with the BP86 functional. The calculated bond lengths and bond angles match reasonably well with the experimental bond lengths obtained from single-crystal X-ray diffraction studies (Table S2 (Supporting Information)). A look at the spin densities calculated according to the Löwdin population analysis shows that for both $\mathbf{1}^{\bullet-}$ and $\mathbf{2}^{\bullet-}$ the spin is equally distributed between the $\text{L}^{\text{1}-\text{H}}$ and the two az_{H} ligands (Figure 4). For $\mathbf{1}^{\bullet-}$ 45% spin density is localized on the bridging $\text{L}^{\text{1}-\text{H}}$ ligand and 58% spin density is distributed between the two az_{H} ligands. For the platinum complex $\mathbf{2}^{\bullet-}$ 60% spin density is on $\text{L}^{\text{1}-\text{H}}$ and the two az_{H} ligands together account for 41% of the spin density. Small amounts of negative spin density are also observed at the central C atoms of the $\text{L}^{\text{1}-\text{H}}$ ligands and at the metal centers. The calculated g values are 1.991 and 1.961 for $\mathbf{1}^{\bullet-}$ and $\mathbf{2}^{\bullet-}$, respectively, and match reasonably well with the experimental values. Thus, it is seen that spin densities for both calculated complexes are predominantly located on all three ligands. The distribution of the spin density on all three ligands that contain many different nuclei with nuclear spins, combined with the narrow width of the signals, is possibly the reason that the expected hyperfine splittings in the experimental EPR spectra of these complexes are not observed.

UV-Vis-Near-IR Spectroelectrochemistry and TD-DFT Calculations. The Pd(II) complex **1**, which contains the $\text{L}^{\text{1}-\text{H}}$ bridge with a $[\text{O},\text{N},\text{O},\text{N}]$ donor set, shows the main absorption bands at 493, 486, 366, and 308 nm in THF (Figure 5 and Table 3). A weak band in the longer wavelength region and two intraligand transitions at higher energies are observed as well (Figure 5). The Pt(II) analogue **2**, with the same ligand sets, displays a similar spectrum, albeit with the intense long-wavelength bands shifted to lower energies (Figure 5). Remarkably, the absorptions in the visible region are highly intense with extinction coefficients exceeding $150000 \text{ M}^{-1} \text{ cm}^{-1}$. Such high extinction coefficients are a result of extensively delocalized systems that lead to optimal orbital overlap, resulting in large oscillator strengths (vide infra). Alternatively, a large transition dipole moment may be responsible for these high extinction coefficient values. The Pt(II) complex **3**, that has $\text{L}^{\text{2}-\text{H}}$ with a $[\text{N},\text{N},\text{N},\text{N}]$ donor set as a bridge,

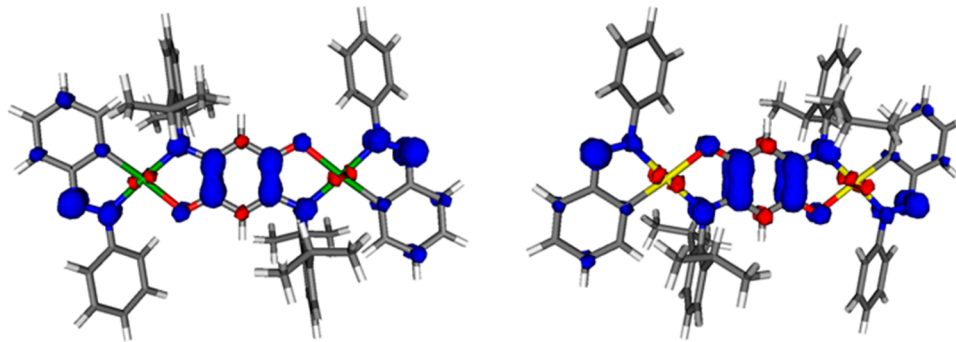


Figure 4. Spin density plots for **1^{•-}** (left) and **2^{•-}** (right).

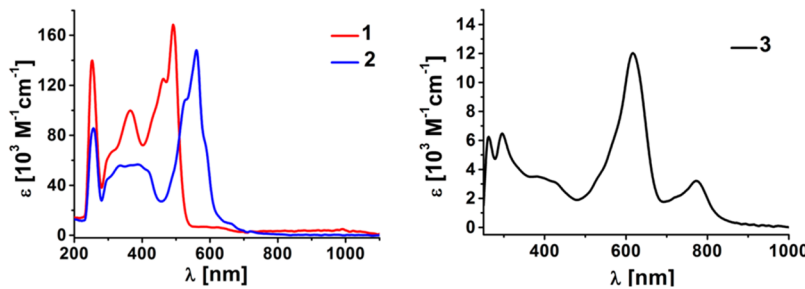


Figure 5. UV–vis spectra of **1–3** in THF.

Table 3. UV–Vis–Near-IR Data of the Investigated Complexes^a

	λ (nm) (ϵ ($10^3 \text{ M}^{-1} \text{ cm}^{-1}$))
[1] ⁰	225 (243.9); 244 sh; 308 (70.4); 366 (102.4); 433 sh; 486 (164.2); 493 (173.3); 588 (4.4)
[1] ^{•-}	226 (246.2); 245 sh; 317 sh; 370 (93.7); 462 (94.7); 486 (105.3); 493 (106.9); 607 (23.5); 647 (28.8); 1596 (3.8); 2427 (19.0)
[1] ²⁻	226 (251.6); 279 sh; 430 (97.2); 608 (31.6); 645 (36.6); 1640 (8.3); 2431 (24.8)
[1] ³⁻	226 (259.3); 277 (108.0); 335 sh; 433 (139.0); 586 (33.0); 631 (33.7); 1323 (22.2)
[2] ⁰	225 (186.8); 223 sh; 298 (56.5); 333 (64.9); 366 (64.5); 384 (63.8); 420 sh; 527 (114.3); 562 (154.4); 586 sh; 701 (7.5)
[2] ^{•-}	225 (183.5); 273 sh; 358 (68.3); 419 sh; 518 (21.4); 671 sh; 702 (101.0); 736 (65.3); 1174 (11.6); 1429 (24.4); 1715 (45.3)
[2] ²⁻	225 (184.1); 274 sh; 308 sh; 353 sh; 474 (34.3); 557 sh; 791 (8.5); 1504 (185.7)
[2] ³⁻	226 (193.9); 278 sh; 377 (69.8); 475 sh; 1021 sh; 1115 (122.8); 1329 sh; 1501 (48.0)
[3] ⁰	209 (22.7); 225 sh; 251 sh; 292 (8.3); 422 (3.8); 619 (18.5); 776 (1.8); 983 (0.6)
[3] ^{•-}	209 (25.3); 225 sh; 258 sh; 312 sh; 418 (3.8); 620 (3.2); 770 (15.2); 1461 (1.9); 1871 (6.0)
[3] ²⁻	210 (28.1); 228 sh; 257 sh; 305 sh; 389 (5.5); 495 (4.0); 586 (3.0); 775 (3.2); 1351 (12.5); 1860 (1.3)
[3] ³⁻	210 (32.5); 252 sh; 297 (12.0); 450 sh; 594 (3.3); 1191 (3.3); 1349 sh

^aFrom OTTLE spectroelectrochemistry in THF/0.1 M Bu₄NPF₆.

displays the main absorptions in the visible region at 776, 619, and 422 nm. Thus, the change of the bridging ligand on moving from complex **2** to **3** leads to a low-energy shift of the transitions in the visible region. The continuous shifts of the long-wavelength bands to lower energies in the series **1–3** correlate with the decreasing potential difference between the first oxidation and first reduction steps in the order **1** > **2** > **3** (see Table 2). The extinction coefficients for the absorption bands in **3** are about a factor of 10 smaller in comparison to what is observed for **1** and **2** (Figure 5 and Table 3). This decrease is tentatively attributed to a less favorable orbital overlap in **3** due to the steric bulk of the phenyl substituents

on all the N donors of the bridge L²_{2H}, which possibly leads to lower oscillator strengths.

In order to shed light on the nature of the transitions observed in the UV–vis spectra of these complexes, structure-based TD-DFT calculations were carried out on complexes **1** and **2**. Similar calculations were not attempted on **3**, due to the absence of an experimental crystal structure in combination with the size of that molecule. For both **1** and **2**, the majority contribution to the valence orbitals comes from the bridging ligand L¹_{2H} and the ancillary ligands az_H (Tables S3–S6 (Supporting Information)). The relevant frontier orbitals for the transitions in **1** and **2** are depicted in Figure 6 and Figure S3 (Supporting Information), respectively, and the relevant data are tabulated in Table 4 and Table S7 (Supporting Information).

TD-DFT calculations delivered a mixed origin for most of the transitions observed in these complexes. For **1**, the most intense long wavelength band at 493 nm (calculated 510 nm) is a HOMO-1 → LUMO transition. A look at these orbitals in Figure 6 shows that this transition can be assigned to a mixture of Pd(dπ) to az_H(π*) metal-to-ligand charge transfer (MLCT) transition and a π → π* transition within the L¹_{2H} ligand. The next absorption band at 486 nm (calculated 463 nm) is a mixture of HOMO-5 → LUMO, HOMO-2 → LUMO, and HOMO-1 → LUMO transitions. This transition is thus a mixture of MLCT to both types of ligands, an az_H → L¹_{2H} ligand-to-ligand charge transfer (LLCT) transition and intraligand charge transfer (ILCT) within the L¹_{2H} ligand. Similarly, the broad band with a maximum at 366 nm also has a mixed origin (Table 4).

For the Pt(II) complex **2**, the most intense long-wavelength band is calculated at 517 nm (experimental 527 and 562 nm). This band is a mixture of HOMO-2 → LUMO and HOMO-1 → LUMO transitions (Table S7 and Figure S3 (Supporting Information)). Hence, this transition is a mixture of MLCT to both ligands, az_H → L¹_{2H} LLCT, and a π → π* transition within the L¹_{2H} ligand. As can be seen from Table S6 (Supporting

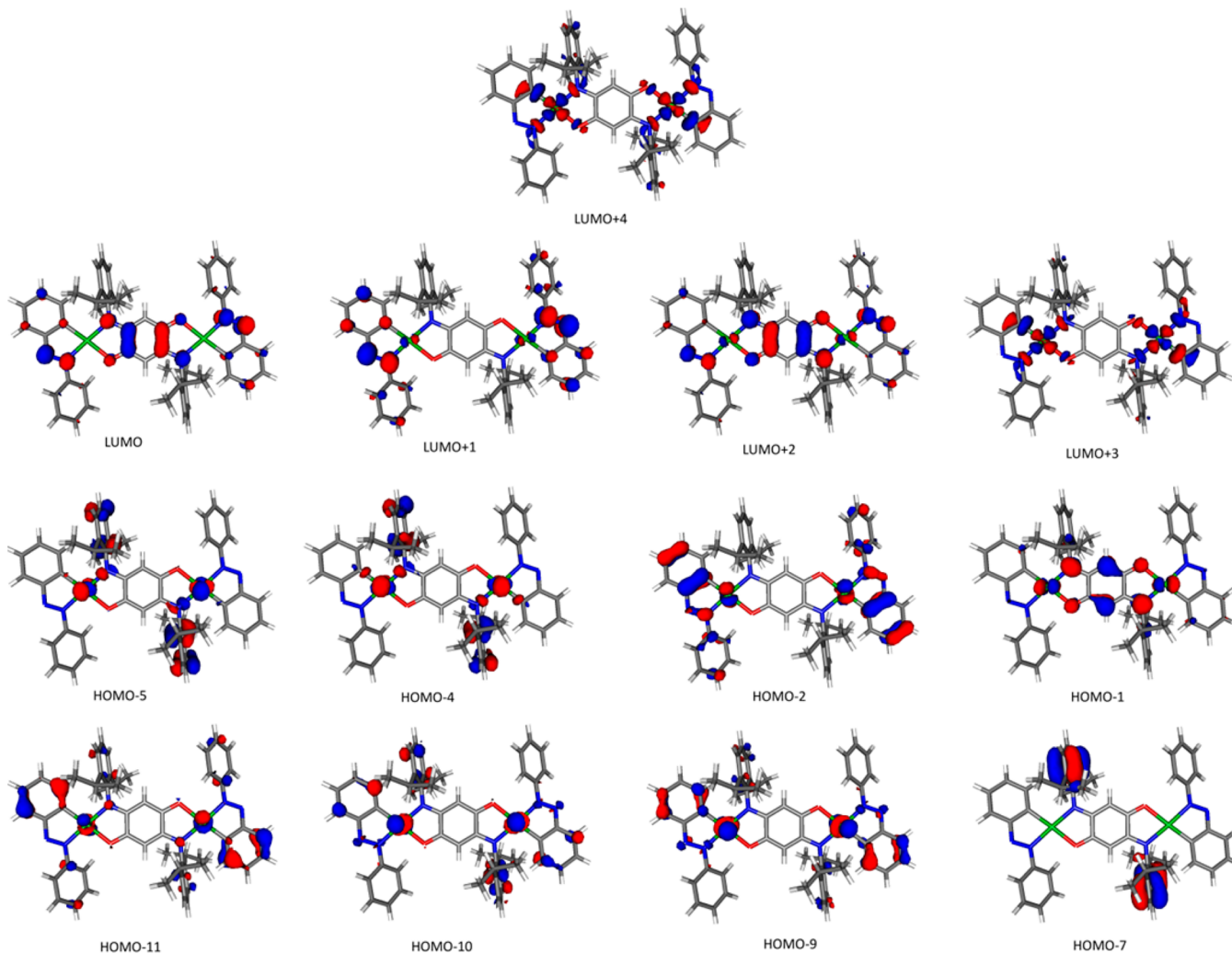


Figure 6. Relevant frontier orbitals for the transitions observed in **1**: canonical orbitals.

Table 4. Main Transitions Obtained from TD-DFT for **1**

main contributing excitation (%)	transition wavelength (nm)	oscillator strength	exptl transition wavelength (nm)	molar abs coeff ($M^{-1} \text{ cm}^{-1}$)
HOMO-1 → LUMO (77)	510	0.457	493	173300
HOMO-5 → LUMO (27)	463	0.213	486	164200
HOMO-2 → LUMO (40)				
HOMO-1 → LUMO (10)				
HOMO-11 → LUMO (22)	390	0.239	366	102400
HOMO-1 → LUMO+2 (35)				
HOMO-10 → LUMO+1 (38)	349	0.228		
HOMO-9 → LUMO+1 (26)				
HOMO-7 → LUMO+2 (18)				
HOMO-2 → LUMO+4 (23)	319	0.211	308	70400
HOMO-4 → LUMO+3 (11)				

Information), all further transitions observed in the visible region are also mixed in character.

One-electron reduction of **1** to **1•-** leads to a loss in intensity of the existing bands of **1**; however, the position of the original bands that are below 500 nm remain largely unchanged (Figure 7, Figure S4 (Supporting Information), and Table 3). In addition, new absorption bands appear for **1•-** at 607 and 647 nm in the visible region and a broad band is generated in the near-IR region. Thus, **1**, which is transparent in the near-IR region, develops a broad absorption band in that region in its one-

electron-reduced **1•-** form (Figure 7). Similar absorptions in the near-IR region are also observed for the one-electron-reduced Pt(II) complexes **2•-** and **3•-** (Figure 7, S5 and S6). The position of the near-IR transition is similar for the Pt(II) complexes **2•-** and **3•-**, whereas that absorption is shifted to lower energies for the Pd(II) complex **1•-**. The complex **2•-** displays the highest intensity for the near-IR transitions (Table 3).

TD-DFT calculations on **1•-** show that the origin of the bands in the visible region is similar to what has been discussed above for the neutral complex **1** (Figure 8 and Table 5). The absorption

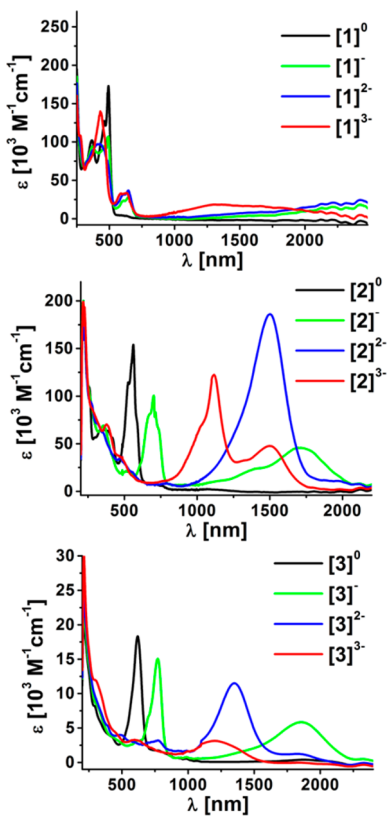


Figure 7. UV–vis–near-IR spectra of complexes **1–3** in the various redox states in THF/0.1 M Bu_4NPF_6 .

observed in the near-IR region for $\mathbf{1}^{\bullet-}$ is a HOMO(α) \rightarrow LUMO(α) transition. The near-IR bands in this case can thus be described as a mixture of predominantly $\text{L}^{\text{I}-\text{H}} \rightarrow \text{az}_{\text{H}}$ LLCT and $\text{L}^{\text{I}-\text{H}} \rightarrow \text{Pd(II)}$ ligand-to-metal charge transfer (LMCT) transitions.

For $\mathbf{2}^{\bullet-}$, the transitions in the visible region are mixed in character, as has been discussed above for **2**. The near-IR band for $\mathbf{2}^{\bullet-}$ is a HOMO(α) \rightarrow LUMO(α) transition. This transition thus has $\text{L}^{\text{I}-\text{H}} \rightarrow \text{az}_{\text{H}}$ LLCT and $\text{L}^{\text{I}-\text{H}} \rightarrow \text{Pt(II)}$ LMCT character (Figure S7 and Table S8 (Supporting Information)).

On further reducing the complex $\mathbf{1}^{\bullet-}$ to $\mathbf{1}^{2-}$, only minimal changes are observed in the visible (Figure 7 and Figure S4 (Supporting Information)) and the near-IR region; the bands just change their intensity while still remaining at similar positions. However, for the Pt(II) complexes $\mathbf{2}^{2-}$ and $\mathbf{3}^{2-}$, the intense bands in the visible region observed for $\mathbf{2}^{\bullet-}$ and $\mathbf{3}^{\bullet-}$ completely lose their intensity (Figure 7 and Figures S5 and S6 (Supporting Information)). Additionally, the near-IR bands become narrower and appear at 1504 and 1351 nm for $\mathbf{2}^{2-}$ and $\mathbf{3}^{2-}$, respectively. Remarkably, the transition at 1504 nm for $\mathbf{2}^{2-}$ has an extinction coefficient of more than $180000 \text{ M}^{-1} \text{ cm}^{-1}$, a value which to the best of our knowledge is one of the largest for near-IR bands observed in transition-metal complexes. Hence reduction of the Pt(II) complexes by a further electron shifts the near-IR bands in their position and also makes them drastically more intense (particularly for $\mathbf{2}^{2-}$). In the absence of reliable TD-DFT calculations for these highly charged species, we can only speculate on their origin. In view of the results obtained for the one-electron-reduced complexes, it would be reasonable to postulate the near-IR transitions in the doubly reduced complexes as a mixture of LLCT and LMCT transitions.

On further reducing the complexes to $\mathbf{1}^{3-}$, $\mathbf{2}^{3-}$, or $\mathbf{3}^{3-}$ only minimum changes are observed in the visible region (Figure 7 and Figures S4–S6 (Supporting Information)). However, the near-IR transitions shift further to higher energies in all three cases and lose intensity for $\mathbf{2}^{3-}$ and $\mathbf{3}^{3-}$ (Table 3 and Figure 7).

CONCLUSIONS

In summary, we have presented here dinuclear Pd(II) and Pt(II) complexes **1** and **2** with an $[\text{O},\text{N},\text{O},\text{N}]$ donor containing bridge $\text{L}^{\text{I}-\text{H}}$ and a dinuclear Pt(II) complex **3** with the doubly deprotonated form of azophenine as a bridge with an $[\text{N},\text{N},\text{N},\text{N}]$ donor set. All complexes additionally contain the redox-active deprotonated azobenzene az_{H} as ancillary ligands. Complex **3** is a rare example of a dinuclear complex with azophenine, a ligand which has become increasingly popular as a bridge. Structural characterization of **1** and **2** has shown a slightly elongated N=N double bond in the az_{H} stoppers owing to back-bonding from the metal centers. Additionally, a localized bonding situation is observed in the quinonoid bridging ligands.

All complexes display an irreversible oxidation step and three reversible reduction steps. The individual redox potentials, as well as the separation between them, are strongly dependent on the nature of the bridge as well as of the metal center. All complexes in their neutral form display strong absorptions in the visible region, the positions of which correlate well with the potential difference between the first oxidation and first reduction steps of the complexes. Stepwise reduction of the complexes leads to the appearance of absorption bands in the near-IR region, the position and intensity of which can be controlled by the redox state of the metal complexes. Thus, the metal complexes presented here display strong electrochromic behavior. Remarkably, the diplatinum complex $\mathbf{2}^{2-}$ displays an absorption band in the near-IR region that has an extinction coefficient of more than $180000 \text{ M}^{-1} \text{ cm}^{-1}$, one of the largest values observed for such transitions in metal complexes. A combination of EPR spectroscopy and (TD)DFT calculations has revealed a highly delocalized nature of the frontier orbitals in these metal complexes. It is possibly this delocalization and the resulting extended π systems that make the appearance of highly intense near-IR bands and strongly electrochromic behavior in these metal complexes possible. Our results here show how the judicious combination of several redox-active ligands in combination with square-planar metal centers can be used to generate extended platforms that are redox-rich and highly electrochromic.

EXPERIMENTAL SECTION

General Considerations. Ligands L^{I} and L^{II} and $\text{M}_2\text{az}_{\text{H}}\text{Cl}_2$ ($\text{M} = \text{Pd, Pt}$) were prepared according to reported procedures.^{6,7,11} All other reagents are commercially available and were used as received. All solvents were dried and distilled using common techniques unless otherwise mentioned.

Instrumentation. ^1H and ^{13}C NMR spectra were recorded with JEOL Lambda 400 (400 MHz) and Bruker Avance III 700 (700 MHz) instruments. Cyclic voltammetry was carried out in 0.1 M Bu_4NPF_6 solution using a three-electrode configuration (glassy-carbon working electrode, Pt counter electrode, Ag wire as pseudoreference electrode) and a PAR VersaSTAT 4 (Ametek) potentiostat. The ferrocene/ferrocenium (Fc/Fc^+) couple served as internal reference. UV–vis–near-IR absorption spectra were recorded on an Avantes spectrometer system. UV–vis–near-IR spectroelectrochemical measurements were carried out using an optically transparent thin-layer electrochemical (OTTLE) cell.¹⁴ EPR spectra in the X band were recorded with a Bruker System EMX instrument. Elemental analysis was performed on an

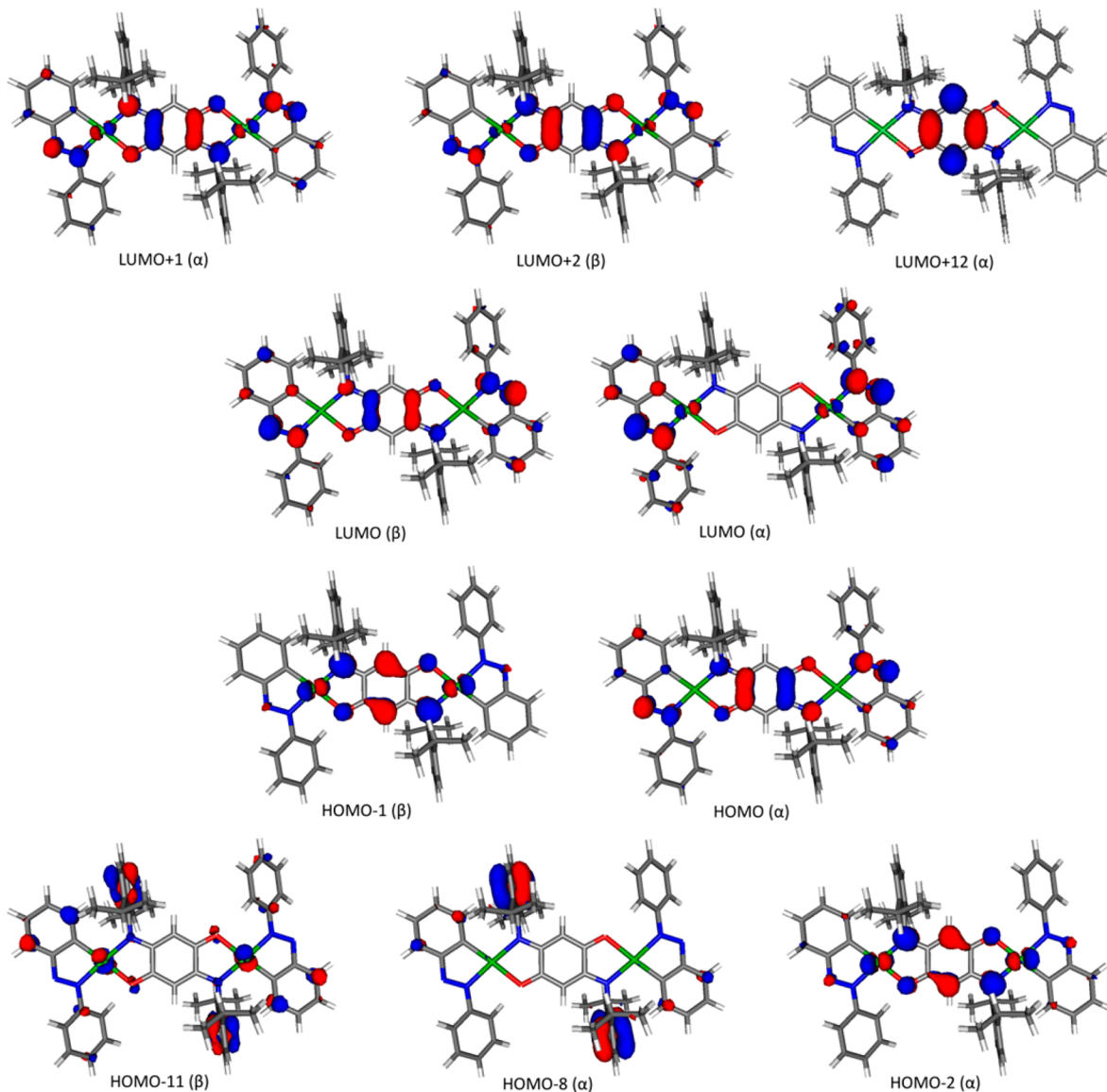


Figure 8. Relevant frontier orbitals for the transitions observed in $1^{\bullet-}$.

Table 5. Main Transitions Obtained from TD-DFT for $1^{\bullet-}$

main contributing excitation (%)	transition wavelength (nm)	oscillator strength	exptl transition wavelength (nm)	molar abs coeff ($M^{-1} \text{ cm}^{-1}$)
HOMO α → LUMO α (92)	1658	0.581	1596	3800
HOMO-2 α → LUMO+1 α (33)	597	0.251	607/647	23500/28800
HOMO-1 β → LUMO β (45)				
HOMO-1 β → LUMO+2 β (14)				
HOMO-2 α → LUMO+1 α (19)	518	0.337	462/486/493	94700/105300/ 106900
HOMO-1 β → LUMO β (39)				
HOMO-1 β → LUMO+2 β (17)				
HOMO-2 α → LUMO+1 α (21)	390	0.137	370	93700
HOMO α → LUMO+12 α (13)				
HOMO-1 β → LUMO+2 β (24)				
HOMO-8 α → LUMO+1 α (40)	358	0.111		
HOMO-11 β → LUMO β (18)				
HOMO α → LUMO+12 α (49)	348	0.112		

Elementar Vario EL III instrument. Mass spectrometry experiments were carried out on an Agilent 6210 ESI-TOF mass spectrometer (Agilent Technologies, Santa Clara, CA, USA).

Synthesis. **Complex 1.** A mixture of L^1 (37 mg, 0.1 mmol), $\text{Pd}_2(\text{az})_2\text{Cl}_2$ (64.5 mg, 0.1 mmol), and NEt_3 (1 mL) in acetonitrile

(15 mL) was stirred for 24 h at room temperature. A brown precipitate was formed. The solid was filtered and washed with acetonitrile (20 mL) and diethyl ether (20 mL). The complex was recrystallized in chloroform/diethyl ether (1/5). Yield: 50 mg (50%). ^1H NMR (400 MHz, CDCl_3): δ 0.99 (d, 6H, $^3J = 6.8 \text{ Hz}$, iPr); 1.19 (d, 6H, $^3J = 6.9 \text{ Hz}$, iPr); 3.23 (sept, 2H,

$^3J = 6.7$ Hz, iPr); 4.99 (s, 1H, quinone); 6.71 (m, 1H); 7.04 (dt, 1H, $^3J = 7.5$ Hz, $^4J = 1.1$ Hz, azobenzene); 7.27 (m, 2H); 7.38 (m, 1H); 7.45 (m, 3H); 8.81 (dd, 1H, $J = 7.6$ Hz, $J = 1.5$ Hz); 8.01 (m, 2H). ^{13}C NMR (175 MHz, CDCl_3): δ 177.60; 173.10; 164.42; 154.87; 151.72; 142.50; 142.34; 132.43; 132.35; 131.12; 130.28; 129.42; 128.62; 127.11; 125.52; 123.93; 97.62; 65.86; 28.04; 24.12; 23.06. Anal. Calcd for $\text{C}_{54}\text{H}_{54}\text{N}_6\text{O}_2\text{Pd}_2$: C, 62.85; H, 5.27; N, 8.14. Found: C, 62.52; H, 5.50; N, 8.24. HRMS (ESI): calcd for $\text{C}_{54}\text{H}_{55}\text{N}_6\text{O}_2\text{Pd}_2$ ([M + H] $^+$) m/z 1033.2477; found 1033.2537.

Complex 2. A mixture of L^1 (37 mg, 0.1 mmol), $\text{Pt}_2(\text{az})_2\text{Cl}_2$ (82.0 mg, 0.1 mmol), and NEt_3 (1 mL) in acetonitrile (15 mL) was stirred for 24 h at room temperature. A violet solution was formed. The solvent was evaporated, and the raw product was purified by column chromatography on Al_2O_3 with dichloromethane/pentane (1/5). The complex was recrystallized in dichloromethane/methanol (1/7). The complex was obtained as a deep violet solid. Yield: 31 mg (30%). ^1H NMR (400 MHz, CDCl_3): δ 1.00 (d, 6H, $^3J = 6.8$ Hz, iPr); 1.18 (d, 6H, $^3J = 6.8$ Hz, iPr); 3.18 (sept, 2H, $^3J = 6.8$ Hz, iPr); 5.07 (s, 1H, quinone); 6.77 (m, 1H); 6.08 (m, 1H); 7.33 (m, 1H); 7.47 (m, 5H); 7.92 (m, 4H). ^{13}C NMR (100 MHz, CDCl_3) δ 178.80, 173.34, 164.78, 151.71, 142.83, 142.27, 139.16, 131.92, 131.19, 130.87, 128.99, 128.49, 127.94, 124.46, 124.35, 124.20, 100.00, 97.57, 27.97, 24.22, 23.36. Anal. Calcd for $\text{C}_{54}\text{H}_{54}\text{N}_6\text{O}_2\text{Pt}_2 \cdot \text{C}_5\text{H}_{12}$: C, 55.30; H, 5.19; N, 6.56. Found: C, 54.91; H, 5.44; N, 5.82. HRMS (ESI): calcd for $\text{C}_{54}\text{H}_{55}\text{N}_6\text{O}_2\text{Pt}_2$ ([M + H] $^+$) m/z 1209.3682; found 1209.3581.

Complex 3. A mixture of L^2 (21 mg, 0.05 mmol), $\text{Pt}_2(\text{az})_2\text{Cl}_2$ (41.0 mg, 0.05 mmol), and NEt_3 (1 mL) in acetonitrile (15 mL) was refluxed for 6 h. A blue solution was formed. The solvent was evaporated, and the raw product was purified by column chromatography on Al_2O_3 with dichloromethane. The complex was recrystallized in dichloromethane/hexane (1/3). The complex was obtained as a deep blue solid. Yield: 15 mg (24%). ^1H NMR (400 MHz, CD_2Cl_2): δ 4.62 (s, 2H); 5.52 (m, 2H); 6.69 (m, 6H); 6.78 (m, 4H); 6.94 (m, 6H); 7.03 (m, 4H); 7.15 (m, 6H); 7.27 (m, 8H); 7.83 (m, 2H). Anal. Calcd for $\text{C}_{54}\text{H}_{40}\text{N}_8\text{Pt}_2 \cdot \text{CH}_2\text{Cl}_2$: C, 51.77; H, 3.32; N, 8.78. Found: C, 51.98; H, 4.02; N, 8.54. HRMS (ESI): calcd for $\text{C}_{54}\text{H}_{41}\text{N}_8\text{Pt}_2$ ([M + H] $^+$) m/z 1191.2741; found 1191.2699.

X-ray Crystallography. Single crystals of **1·2Et₂O** were obtained by the slow diffusion of diethyl ether into a chloroform solution of **1**. Single crystals of **2** were obtained by layering a dichloromethane solution of **2** with methanol and allowing for slow diffusion at ambient temperature. Intensity data were collected at 200(2) K on a Stoe X-Area diffractometer for **1·2Et₂O** and at 100(2) K on a Bruker Smart AXS diffractometer for **2** (graphite-monochromated Mo K α radiation, $\lambda = 0.71073$ Å). Crystallographic and experimental details for the structures are summarized in Table S1 (Supporting Information). Structures were solved by direct methods (SHELXS-97) and refined by full-matrix least-squares procedures (based on F^2 , SHELXL-97).¹⁵ CCDC 964896 and 964897 contain CIF files for these structures. All data can be obtained free of charge from the Cambridge Crystallographic Data Centre via www.ccdc.cam.ac.uk/data_requests/cif.

DFT Calculations. DFT calculations were performed with the ORCA 2.9.1 program package¹⁶ using the BP86 and B3LYP functionals for the geometry optimization and single-point calculations, respectively.¹⁷ Empirical van der Waals corrections were utilized for the geometry optimization.¹⁸ Default convergence criteria were set for the geometry-optimization (OPT) and tight convergence criteria for SCF calculations (TIGHTSCF). Relativistic effects were included with the zeroth-order relativistic approximation (ZORA).¹⁹ Triple- ζ valence basis sets with polarization functions (TZVPP-ZORA)²⁰ were employed for all atoms. The resolution of the identity approximation²¹ was used with matching auxiliary basis sets. Time-dependent DFT (TD-DFT) was employed to calculate the low-lying excitation energies. Solvent effects were taken into account with the conductor-like screening model (COSMO)²² for all calculations. Spin densities were calculated according to the Löwdin population analysis.²³ The contribution of molecular fragments to molecular orbitals was analyzed with the MOAnalyzer tool.²⁴ Molecular orbitals and spin densities were visualized with the Molekel program.²⁵

ASSOCIATED CONTENT

Supporting Information

Figures, tables, and CIF and .xyz files giving details of DFT calculations, CVs of complexes in dcm, EPR spectrum of **1^{•-}**, DFT calculated frontier orbitals of **2** and **2^{•-}**, UV-vis-near-IR spectroelectrochemical data for **1–3**, crystallographic data for **1·2Et₂O** and **2**, comparison of calculated and experimental bond lengths and bond angles for **1** and **2**, frontier orbital compositions of **1**, **1^{•-}**, **2**, and **2^{•-}**, and main DFT transitions for **2** and **2^{•-}**. This material is available free of charge via the Internet at <http://pubs.acs.org>.

AUTHOR INFORMATION

Corresponding Author

*E-mail for B.S.: Biprajit.sarkar@fu-berlin.de.

Notes

The authors declare no competing financial interest.

ACKNOWLEDGMENTS

We are indebted to the Carl-Zeiss Stiftung (doctoral stipend for N.D.) and the Fonds der Chemischen Industrie (Chemiefondsstipendium for M.G.S.) for the financial support of this project. The ZEDAT, FU Berlin, is acknowledged for access to the computing center. We are grateful to Dr. A. Hagenbach for the measurement of the crystals of **1**.

REFERENCES

- (a) Forum Issue on Redox-Active Ligands: *Inorg. Chem.* **2011**, *50*, 9737–9914. (b) Cluster Issue, Cooperative and Redox Non-Innocent Ligands in Directing Organometallic Reactivity: *Eur. J. Inorg. Chem.* **2012**, *340*–580.
- (2) For selected examples see: (a) Ward, M. D.; McCleverty, J. A. *Dalton Trans.* **2002**, 275. (b) Pierpont, C. G. *Coord. Chem. Rev.* **2001**, 216–217, 95. (c) Zanello, P. *Coord. Chem. Rev.* **2006**, *50*, 2000. (d) de Bruin, B.; Hetterscheid, D. G. H.; Koekkoek, A. J. J.; Grützmacher, H. *Prog. Inorg. Chem.* **2007**, *55*, 247. (e) Poddel'sky, A. I.; Cherkasov, V. K.; Abakumov, G. A. *Coord. Chem. Rev.* **2009**, *293*, 291. (f) Chaudhuri, P.; Verani, C. N.; Bill, E.; Weyhermüller, T.; Neese, F.; Wieghardt, K. *J. Am. Chem. Soc.* **2001**, *123*, 2213. (g) Bhattacharya, S.; Gupta, P.; Basuli, F.; Pierpont, C. G. *Inorg. Chem.* **2002**, *41*, 5810. (h) Sarkar, B.; Huebner, R.; Pattacini, R.; Hartenbach, I. *Dalton Trans.* **2009**, 4653. (i) Deibel, N.; Schweinfurth, D.; Fiedler, J.; Zalis, S.; Sarkar, B. *Dalton Trans.* **2011**, *40*, 9925. (j) Paretzki, A.; Das, H. S.; Weisser, F.; Scherer, T.; Bubrin, D.; Fiedler, J.; Nyicz, J. E.; Sarkar, B. *Eur. J. Inorg. Chem.* **2011**, 2413. (k) Nomura, M.; Cauchy, T.; Fourmigüé, M. *Coord. Chem. Rev.* **2010**, *254*, 1406. (l) Bonneval, B. G. d.; Ching, K. I. M. C.; Alary, F.; Bui, T.-T.; Valade, L. *Coord. Chem. Rev.* **2010**, *254*, 1457.
- (3) For selected examples see: (a) Chirik, P. J.; Wieghardt, K. *Science* **2010**, *327*, 794. (b) Ringenberg, M. R.; Kokatam, S. L.; Heiden, Z. M.; Rauchfuss, T. B. *J. Am. Chem. Soc.* **2008**, *130*, 788. (c) Praneeth, V. K. K.; Ringenberg, M. R.; Ward, T. R. *Angew. Chem.* **2012**, *124*, 10374. (d) Dzik, W. I.; van der Vlugt, J. I.; Reek, J. N. H.; de Bruin, B. *Angew. Chem.* **2011**, *123*, 3416. (e) Nguyen, A. I.; Blackmore, K. J.; Carter, S. M.; Zarkesh, R. A.; Heyduk, A. F. *J. Am. Chem. Soc.* **2009**, *131*, 3307. (f) Tsai, M. K.; Rochford, J.; Polyansky, D. E.; Wada, T.; Tanaka, K.; Muckerman, J. T. *Inorg. Chem.* **2009**, *48*, 4372. (g) Deibel, N.; Schweinfurth, D.; Hohloch, S.; Fiedler, J.; Sarkar, B. *Chem. Commun.* **2012**, *48*, 2388. (h) Lyaskovskyy, V.; de Bruin, B. *ACS Catal.* **2012**, *2*, 270. (i) Deibel, N.; Schweinfurth, D.; Hohloch, S.; Delor, M.; Sazanovich, I. V.; Towrie, M.; Weinstein, J. A.; Sarkar, B. *Inorg. Chem.* **2014**, *53*, 1021.
- (4) For selected examples see: (a) Ward, M. D. *Inorg. Chem.* **1996**, *35*, 1712. (b) Leschke, M.; Melter, M.; Lang, H. *Inorg. Chim. Acta* **2003**, *350*, 114. (c) Kitagawa, S.; Kawata, S. *Coord. Chem. Rev.* **2002**, *224*, 11. (d) Carbonera, C.; Dei, A.; Letard, J.-F.; Sangregorio, C.; Sorace, L. *Angew. Chem., Int. Ed.* **2004**, *43*, 3136. (e) Miller, J. S.; Min, K. S. *Angew.*

- Chem., Int. Ed.* **2009**, *48*, 262. (f) Therrien, B.; Süss-Fink, G.; Govindaswamy, P.; Renfrew, A. K.; Dyson, P. J. *Angew. Chem.* **2008**, *120*, 3833. (g) Heinze, K.; Huttner, G.; Walter, O. *Eur. J. Inorg. Chem.* **1999**, 593. (h) Gallert, S.; Weyhermüller, T.; Wieghardt, K.; Chaudhuri, P. *Inorg. Chim. Acta* **1998**, *274*, 111. (i) Elduque, A.; Garcés, Y.; Oro, L. A.; Pinillos, M. T.; Tiripicchio, A.; Uguzzoli, F. *J. Chem. Soc., Dalton Trans.* **1996**, 2155. (j) Han, Y.-F.; Jia, W.-G.; Yu, W.-B.; Jin, G.-X. *Chem. Soc. Rev.* **2009**, *38*, 3419. (k) Han, Y.-F.; Li, H.; Jin, G.-X. *Chem. Commun.* **2010**, *46*, 6879. (l) Jung, H.; Dubey, A.; Koo, H. J.; Vajpayee, V.; Cook, T. R.; Kim, H.; Kang, S. C.; Stang, P. J.; Chi, K.-W. *Chem. Eur. J.* **2013**, *19*, 6709.
- (5) (a) Das, H. S.; Weisser, F.; Schweinfurth, D.; Su, C.-Y.; Bogani, L.; Fiedler, J.; Sarkar, B. *Chem. Eur. J.* **2010**, *16*, 2977. (b) Schweinfurth, D.; Das, H. S.; Weisser, F.; Bubrin, D.; Sarkar, B. *Inorg. Chem.* **2011**, *50*, 1150. (c) Weisser, F.; Huebner, R.; Schweinfurth, D.; Sarkar, B. *Chem. Eur. J.* **2011**, *17*, 5727. (d) Sommer, M. G.; Schweinfurth, D.; Weisser, F.; Hohloch, S.; Sarkar, B. *Organometallics* **2013**, *32*, 2069. (e) Schweinfurth, D.; Khusniyarov, M. M.; Bubrin, D.; Hohloch, S.; Su, C.-Y.; Sarkar, B. *Inorg. Chem.* **2013**, *52*, 10332. (f) Das, H. S.; Das, A. K.; Pattacini, R.; Huebner, R.; Sarkar, B.; Braunstein, P. *Chem. Commun.* **2009**, 4387. (g) Braunstein, P.; Bubrin, D.; Sarkar, B. *Inorg. Chem.* **2009**, *48*, 2534. (h) Paretzki, A.; Pattacini, R.; Huebner, R.; Braunstein, P.; Sarkar, B. *Chem. Commun.* **2010**, *46*, 1497. (i) Deibel, N.; Schweinfurth, D.; Huebner, R.; Braunstein, P.; Sarkar, B. *Dalton Trans.* **2011**, *40*, 431. (j) Hohloch, S.; Braunstein, P.; Sarkar, B. *Eur. J. Inorg. Chem.* **2012**, 546. (k) Deibel, N.; Hohloch, S.; Sommer, M. G.; Schweinfurth, D.; Ehret, F.; Braunstein, P.; Sarkar, B. *Organometallics* **2013**, *32*, 7366.
- (6) For selected examples see: (a) Braunstein, P.; Siri, O.; Taquet, J.-P.; Rohmer, M.-M.; Bénard, M.; Walter, R. *J. Am. Chem. Soc.* **2003**, *125*, 12246. (b) Yang, Q.-Z.; Siri, O.; Braunstein, P. *Chem. Commun.* **2005**, 2660. (c) Yang, Q.-Z.; Siri, O.; Braunstein, P. *Chem. Eur. J.* **2005**, *11*, 7237. (d) Siri, O.; Taquet, J.-P.; Collin, J.-P.; Rohmer, M.-M.; Bénard, M.; Braunstein, P. *Chem. Eur. J.* **2005**, *11*, 7247. (e) Cotton, F. A.; Jin, J.-Y.; Li, Z.; Murillo, C. A.; Reibenspies, J. H. *Chem. Commun.* **2008**, 211. (f) Kumbhakar, D.; Sarkar, B.; Maji, S.; Mobin, S.; Fiedler, J.; Aparicio, R. J.; Kaim, W.; Lahiri, G. K. *J. Am. Chem. Soc.* **2008**, *130*, 17575. (g) Keyer, T. E.; Forster, R. J.; Jayaweera, P. M.; Coates, C. G.; McGarvey, J. J.; Vos, J. G. *Inorg. Chem.* **1998**, *37*, 5925. (h) Kar, S.; Sarkar, B.; Ghumaan, S.; Janardanan, D.; van Slageren, J.; Fiedler, J.; Puranik, V. G.; Sunoj, R. B.; Kaim, W.; Lahiri, G. K. *Chem. Eur. J.* **2005**, *11*, 4901. (i) Zhang, D.; Jin, G.-X. *Organometallics* **2003**, *22*, 2851. (j) Scheuermann, S.; Kretz, T.; Vitze, H.; Bats, J. W.; Bolte, M.; Lerner, H. W.; Wagner, M. *Chem. Eur. J.* **2008**, *14*, 2590. (k) Mattsson, J.; Govindaswamy, P.; Renfrew, A. K.; Dyson, P. J.; Stepnicka, P.; Süss-Fink, G.; Therrien, B. *Organometallics* **2009**, *28*, 4350. (l) Margraf, G.; Kretz, T.; de Biani, F. F.; Lasi, F.; Loschi, S.; Zanello, P.; Bats, J. W.; Wolf, J.; Removic-Langer, K.; Lang, M.; Prokofiev, A.; Assmus, W.; Lerner, H.-W.; Wagner, M. *Inorg. Chem.* **2006**, *45*, 1277. (m) Su, Y.; Zhao, Y.; Gao, J.; Dong, Q.; Wu, B.; Yang, X.-J. *Inorg. Chem.* **2012**, *51*, 5889. (n) Nawn, G.; McDonald, R.; Hicks, R. G. *Inorg. Chem.* **2013**, *52*, 10912.
- (7) Ruggli, P.; Buchmeier, F. *Helv. Chim. Acta* **1945**, *28* (1), 850.
- (8) (a) Rall, J.; Stange, A. F.; Hübler, K.; Kaim, W. *Angew. Chem., Int. Ed.* **1998**, *37*, 2681. (b) Siri, O.; Braunstein, P.; Taquet, J.-P.; Collin, J.-P.; Welter, R. *Dalton Trans.* **2007**, 1481. (c) Siri, O.; Braunstein, P.; Rohmer, M.-M.; Bénard, M.; Welter, R. *J. Am. Chem. Soc.* **2003**, *125*, 13793. (d) Frantz, S.; Rall, J.; Hartenbach, I.; Schleid, T.; Zalis, S.; Kaim, W. *Chem. Eur. J.* **2004**, *10*, 149. (e) Jeon, I.-R.; Park, J. G.; Xiao, D. J.; Harris, T. D. *J. Am. Chem. Soc.* **2013**, *135*, 16845.
- (9) (a) Kaim, W. *Coord. Chem. Rev.* **2011**, *255*, 2503. (b) Chen, J.; Winter, R. F. *Chem. Eur. J.* **2012**, *18*, 10733. (c) Ward, M. D. *J. Solid State Electrochem.* **2005**, *9*, 778. (d) Mortimer, R. J. *Compr. Coord. Chem.* **2004**, *9*, 581. (e) Polit, W.; Exner, T.; Wuttke, E.; Winter, R. F. *Bioinorg. React. Mech.* **2012**, *8*, 85.
- (10) For selected examples see: (a) Yukuta, T.; Mori, I.; Kurihara, M.; Mizutani, J.; Tamai, N.; Kawai, T.; Irie, M.; Nishihara, H. *Inorg. Chem.* **2002**, *41*, 7143. (b) Kume, S.; Nishihara, H. *Dalton Trans.* **2008**, 3260. (c) Hirade, T.; Okui, Y.; Han, M. N. *J. Mater. Chem. C* **2013**, *1*, 2672. (d) Babic, D.; Curic, M.; Molcanov, K.; Ilc, G.; Plavec, J. *Inorg. Chem.* **2008**, *47*, 10446. (e) Roy, S.; Hartenbach, I.; Sarkar, B. *Eur. J. Inorg. Chem.* **2009**, 2553. (f) Moustafa, M. E.; McCready, M. S.; Pudephatt, R. J. *Organometallics* **2012**, *31*, 6262. (g) Juribasic, M.; Curic, M.; Molcanov, K.; Matkovic-Calogovic, D.; Babic, D. *Dalton Trans.* **2010**, *39*, 8769. (h) Han, M.; Hirade, T.; Hara, M. *New J. Chem.* **2010**, *34*, 2887. (i) Yamamoto, Y.; Yamazaki, H. *J. Org. Chem.* **1977**, *42*, 4136. (j) Bennett, R. L.; Bruce, M. I.; Goodall, B. L.; Stone, F. G. A. *Aust. J. Chem.* **1974**, *27*, 2131. (k) Siedle, A. R. *J. Organomet. Chem.* **1981**, *208*, 115. (l) Bruce, M. I.; Liddell, M. J.; Snow, M. R.; Tiekkink, E. R. T. *Aust. J. Chem.* **1988**, *41*, 1407. (m) Evans, W. J.; Drummond, D. K.; Chamberlain, L. R.; Doedens, R. J.; Bott, S. G.; Zhang, H.; Atwood, J. L. *J. Am. Chem. Soc.* **1988**, *110*, 4983. (n) Zhambrano, C. H.; Sharp, P. R.; Barnes, C. L. *Organometallics* **1995**, *14*, 3607. (o) Curic, M.; Babic, D.; Visnjevac, A.; Molcanov, K. *Inorg. Chem.* **2005**, *44*, 5975. (p) Hoover, J. M.; Freudenthal, J.; Michael, F. E.; Mayer, J. M. *Organometallics* **2008**, *27*, 2238. (q) Cincic, D.; Juribasic, M.; Babic, D.; Molcanov, K.; Sket, P.; Plavec, J.; Curic, M. *Chem. Commun.* **2011**, *47*, 11543. (r) Juribasic, M.; Budimir, A.; Kazazic, S.; Curic, M. *Inorg. Chem.* **2013**, *52*, 12749.
- (11) Cope, A. C.; Siekman, R. W. *J. Am. Chem. Soc.* **1965**, *87*, 3272.
- (12) Connally, N. G.; Geiger, W. E. *Chem. Rev.* **1996**, *96*, 877.
- (13) Patra, S.; Sarkar, B.; Mobin, S. M.; Kaim, W.; Lahiri, G. K. *Inorg. Chem.* **2003**, *42*, 6469.
- (14) Krejcik, M.; Danek, M.; Hartl, F. *J. Electroanal. Chem.* **1991**, *317*, 179.
- (15) Sheldrick, G. M. *SHELXL-97, Program for refinement of crystal structures*; University of Göttingen, Göttingen, Germany, 1997.
- (16) Neese, F. *ORCA—an Ab Initio, Density Functional and Semiempirical Program Package, version 2.9.1*; Department of molecular theory and spectroscopy, Max Planck Institute for Bioinorganic Chemistry, Mühlheim/Ruhr, Germany, January 2012.
- (17) (a) Becke, A. D. *J. Chem. Phys.* **1993**, *98*, 5648. (b) Becke, A. D. *Phys. Rev. A* **1988**, *38*, 3098. (c) Lee, C.; Yang, W.; Parr, R. G. *Phys. Rev. B* **1988**, *37*, 785.
- (18) Grimme, S.; Antony, J.; Ehrlich, S.; Krieg, H. *J. Chem. Phys.* **2010**, *132*, 154104.
- (19) van Wüllen, C. *J. Chem. Phys.* **1998**, *109*, 392.
- (20) Pantazis, D. A.; Chen, X.-Y.; Landis, C. R.; Neese, F. *J. Chem. Theory Comput.* **2008**, *4*, 908.
- (21) (a) Neese, F. *J. Comput. Chem.* **2003**, *24*, 1740. (b) Neese, F.; Wennmohs, F.; Hansen, A.; Becker, U. *Chem. Phys.* **2009**, *356*, 98. (c) Vahtras, O.; Almlöf, J.; Feyereisen, M. W. *Chem. Phys. Lett.* **1993**, *213*, 514. (d) Whitten, J. L. *J. Chem. Phys.* **1973**, *58*, 4496.
- (22) (a) Klamt, A.; Schüürmann, G. *J. Chem. Soc., Perkin Trans. 2* **1993**, *799*. (b) Sinnecker, S.; Rajendran, A.; Klamt, A.; Diedenhofen, M.; Neese, F. *J. Phys. Chem. A* **2006**, *110*, 2235.
- (23) Löwdin, P.-O. *J. Chem. Phys.* **1950**, *18*, 365.
- (24) Delgado-Jaime, M. U.; DeBeer, S. *J. Comput. Chem.* **2012**, *33*, 2180.
- (25) Portmann, S. *Molekel*, version 5.4.0.8; CSCS/UNI, Geneva, Switzerland, 2009.